Evaluation of three-dimensional finite element-based deformable registration of pre- and intraoperative prostate imaging

Aditya Bharatha, Masanori Hirose, Nobuhiko Hata, Simon K. Warfield, Matthieu Ferrant, Kelly H. Zou, Eduardo Suarez-Santana, Juan Ruiz-Alzola, Anthony D'Amico, Robert A. Cormack, Ron Kikinis, Ferenc A. Jolesz, and Clare M. C. Tempany

Evaluation of three-dimensional finite element-based deformable registration of pre- and intraoperative prostate imaging

Aditya Bharatha
Surgical Planning Laboratory, Department of Radiology, Division of MRI, Brigham and Women's Hospital, Harvard Medical School, 75 Francis Street, Boston, Massachusetts 02115 and University of Toronto Medical School, Toronto, Canada

Masanori Hirose
Department of Radiology, School of Medicine, Showa University, Tokyo, Japan and Surgical Planning Laboratory, Department of Radiology, Brigham and Women's Hospital, Harvard Medical School, 75 Francis Street, Boston, Massachusetts 02115

Nobuhiko Hata and Simon K. Warfield
Surgical Planning Laboratory, Department of Radiology, Division of MRI, Brigham and Women's Hospital, Harvard Medical School, 75 Francis Street, Boston, Massachusetts 02115

Matthieu Ferrant
Telecommunications Laboratory, Universite catholique de Louvain, Belgium

Kelly H. Zou
Surgical Planning Laboratory, Department of Radiology, Division of MRI, Brigham and Women's Hospital and Department of Health Care Policy, Harvard Medical School, Boston Massachusetts

Eduardo Suarez-Santana and Juan Ruiz-Alzola
Department of Signals and Communications, University of Las Palmas de Gran Canaria, Spain

Anthony D'Amico, and Robert A. Cormack
Department of Radiation Oncology, Brigham and Women's Hospital and Department of Radiation Oncology, Dana Farber Cancer Institute, Harvard Medical School, Boston, Massachusetts

Ron Kikinis, Ferenc A. Jolesz, and Clare M. C. Tempany[a]
Surgical Planning Laboratory, Department of Radiology, Division of MRI, Brigham and Women's Hospital, Harvard Medical School, 75 Francis Street, Boston, Massachusetts 02115

In this report we evaluate an image registration technique that can improve the information content of intraoperative image data by deformable matching of preoperative images. In this study, pretreatment 1.5 tesla (T) magnetic resonance (MR) images of the prostate are registered with 0.5 T intraoperative images. The method involves rigid and nonrigid registration using biomechanical finite element modeling. Preoperative 1.5 T MR imaging is conducted with the patient supine, using an endorectal coil, while intraoperatively, the patient is in the lithotomy position with a rectal obturator in place. We have previously observed that these changes in patient position and rectal filling produce a shape change in the prostate. The registration of 1.5 T preoperative images depicting the prostate substructure [namely central gland (CG) and peripheral zone (PZ)] to 0.5 T intraoperative MR images using this method can facilitate the segmentation of the substructure of the gland for radiation treatment planning. After creating and validating a dataset of manually segmented glands from images obtained in ten sequential MR-guided brachytherapy cases, we conducted a set of experiments to assess our hypothesis that the proposed registration system can significantly improve the quality of matching of the total gland (TG), CG, and PZ. The results showed that the method statistically–significantly improves the quality of match (compared to rigid registration), raising the Dice similarity coefficient (DSC) from prematched coefficients of 0.81, 0.78, and 0.59 for TG, CG, and PZ, respectively, to 0.94, 0.86, and 0.76. A point-based measure of registration agreement was also improved by the deformable registration. CG and PZ volumes are not changed by the registration, indicating that the method maintains the biomechanical topology of the prostate. Although this strategy was tested for MRI-guided brachytherapy, the preliminary results from these experiments suggest that it may be applied to other settings such as transrectal ultrasound-guided therapy, where the integration of preoperative MRI may have a significant impact upon treatment planning and guidance. © *2001 American Association of Physicists in Medicine.* [DOI: 10.1118/1.1414009]

INTRODUCTION

Prostate cancer represents a major challenge for modern medicine. It is the most common noncutaneous malignancy diagnosed in men in the U.S.[1] As the second-leading cause of death from cancer in American men, the disease is a significant cause of morbidity and mortality. Currently, three major therapies are available for treating clinically localized disease: radical prostatectomy, external beam radiation therapy, and interstitial radiation delivery (brachytherapy). It has been shown that there are significant side effects that may result from radical surgical or radiation treatment, including genitourinary, gastrointestinal, and sexual dysfunction.[2] These complications represent significant issues because not all those diagnosed will necessarily die from prostate cancer. Thus, a balance between definitive cancer control, the preservation of physiologic function, and the maintenance of quality of life is an important goal. These issues have made highly accurate treatment delivery extremely important in therapy for localized prostate cancer. Indeed, image-guided interventions such as transrectal ultrasound (TRUS)-guided brachytherapy are increasingly performed within the field of radiation oncology and prostate cancer therapy.

A recently developed treatment option is magnetic resonance (MR)-guided brachytherapy, performed in an open-configuration 0.5 tesla (T) interventional MR scanner.[3] This technique combines the superior soft tissue contrast of MR with the flexibility of intraoperative imaging. In our practice, the peripheral zone (PZ) of the prostate is selected to be the clinical target volume (CTV).[3] This system allows for intraoperative I-125 seed placement planning based on a CTV, which is defined using intraoperative T2-weighted fast spin echo (FSE) MR images. During the procedure, fast gradient recalled (FGR) images obtained in near real time (approx. 4 s per image) are used for needle guidance and seed placement. The implant is performed using a perineal template with the patient in the lithotomy position (as it is in conventional TRUS-guided implants).

Although 0.5 T T2-weighted images provide good visualization of the gland,[3] 1.5 T imaging with an endorectal coil provides better spatial resolution and contrast. In particular, the ability to visualize the substructure of the prostate [central gland (CG) and PZ] is much improved.[4,5] Pretreatment 1.5 T images provide detail, allowing accurate definition of the gland, its margins, and in most cases, the tumor, all of which are useful for complete treatment planning. It should be noted that of all modalities, MR imaging of the prostate provides the most optimal imaging not only of the gland and its adjacent structures, but importantly, of its substructure. The quality of MR imaging exceeds that of CT. In particular, CT images cannot accurately define substructure nor can they define the inferior and superior borders of the prostate.

To date, little work has been published with the objective of applying rigid and nonrigid registration systems to prostate images. Most methods employed manual matching using visible landmarks.[6,7] Prior work by van Herk[8] attempted to quantify rigid translation and rotation (without deformation) of the prostate between (proton density) MR and CT imaging

studies. In this study, the position of the patient was always supine, never moving to the lithotomy position as in our study, and the endorectal coil (1.5 T) and rectal obturator (0.5 T) were not employed.

We have found that a significant prostate shape change occurs between preoperative 1.5 T endorectal coil imaging (in which the patient is supine) and intraoperative 0.5 T imaging (with the patient in the lithotomy position). In particular, in the preoperative images, the gland appears to have a smaller anterior–posterior dimension and a wider transverse dimension than in the intraoperative images.[9] These changes in shape likely result from differences in rectal filling and/or patient position necessitated by the procedure. Differences in rectal filling may be explained by the fact that preoperative imaging is performed with an endorectal imaging coil (surrounded by an inflatable balloon) while during MR-guided brachytherapy, a smaller rectal obturator is placed in the rectum (to fix a perineal template).

Our main objective in this study is to evaluate a novel approach for improving the information content of 0.5 T intraoperative images by matching pretreatment 1.5 T images using a finite element model-based deformable registration system. The method, previously presented elsewhere,[10] is suitable for an application in prostate matching, since it attempts to preserve the biomechanical topology of the soft tissue. The matching is performed on MR-guided brachytherapy image data by rigidly and then nonrigidly registering the preoperative 1.5 T images to intraoperative 0.5 T images. Although this strategy was tested on MRI-guided brachytherapy data, it could potentially be applied to other settings such as TRUS-guided therapy, where the integration of preoperative MRI may have a great impact upon treatment planning and guidance. Similar glandular deformations due to patient position and rectal filling may occur with TRUS.

After creating and validating a dataset of manually segmented glands from images obtained in ten sequential MR-guided brachytherapy cases, we conducted a set of experiments to assess our hypothesis that a deformable registration system can significantly improve the match between pre- and intraoperative prostate images.

MATERIALS AND METHODS

Patient selection and imaging protocols

Ten sequential MR-guided brachytherapy patients were identified retrospectively, excluding those who had undergone previous external beam radiation therapy (as this can produce confounding shape and signal intensity changes in the gland). The entry criteria for patients into the MR-guided brachytherapy program at our institution have been previously described.[3]

All patients underwent preoperative 1.5 T MR imaging using an endorectal coil with an integrated pelvic-phased multicoil array (Signa LX, GE Medical Systems, Milwaukee WI). The endorectal coil is a receive-only coil mounted inside a latex balloon, and assumes a diameter of 4–6 cm once inflated in the patient's rectum). The patient is placed supine in the closed-bore magnet for the imaging examination. The
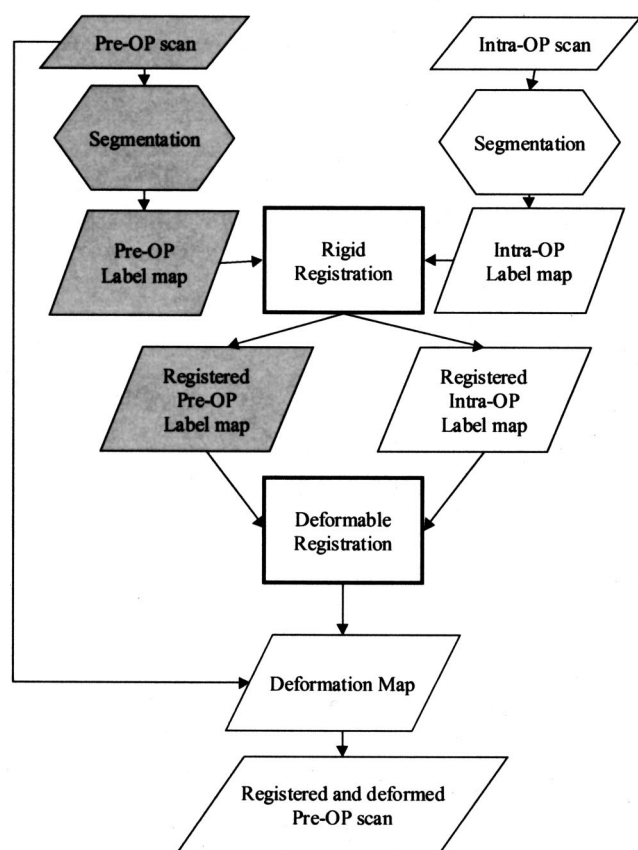
FIG. 1. The process flow chart describing rigid and deformable registration of 1.5 and 0.5 T MRI in prostate brachytherapy.
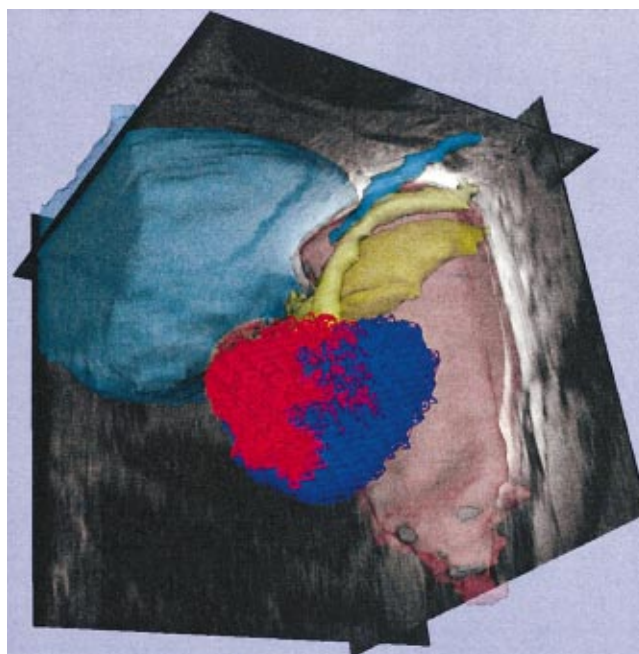

FIG. 2. Three-dimensional mesh representation of the finite element model of CG (red) and PZ (dark blue) of the prostate, shown against normal pelvic anatomy on 1.5 T MR imaging [bladder and ureter (blue); vas deferens and seminal vesicles (yellow); and endorectal coil (black) in the rectum (brown)].

1.5 T T2-weighted images were fast spin echo (FSE) images (4050/135, field of view of 12 cm, section thickness of 3 mm, section gap of 0 mm, matrix of 256×256, 3 signal averages). Typical acquisition times are 5–6 min.

Intraoperative imaging was performed in the open-configuration 0.5 T MR scanner (Signa SP, General Electric Medical Systems, Milwaukee, WI), referred to as the Interventional Magnetic Resonance Therapy (MRT) scanner.[11] Each patient was placed in the lithotomy position in order to facilitate prostate brachytherapy via a perineal template. The perineal template is fixed in place by a rectal obturator (2 cm diam). T2-weighted FSE images (axial and coronal, 6400/100, field of view of 24 cm, section thickness of 5 mm, section gap of 0 mm, matrix of 256×256, 2 signal averages) were acquired in the MRT scanner using a flexible external pelvic wraparound coil, with typical acquisition times of 6 min.

Segmentation

The three-dimensional (3-D) Slicer[12] is a surgical simulation and navigation tool that can display multimodality images either two- or three-dimensionally. In this study, the 3-D Slicer was used to facilitate manual segmentation (i.e., contouring) of the CG and PZ of the prostate in T2-weighted images from the 1.5 and 0.5 T studies. The ten cases were randomly divided into two balanced sets, with each set con-

taining five cases. Each set was assigned to an operator. For the assessment of reliability of segmentation, the operator independently and blindly segmented the 1.5 and 0.5 T datasets five times in random sequence. In segmenting the 0.5 T datasets, the operator was permitted to refer to preoperative (1.5 T) scans, in accordance with actual brachytherapy sessions.

Image registration strategy

A software system was developed to automate the process of first rigid and then nonrigid registration of the image datasets (Fig. 1). In order to apply deformable registration, a rigid registration step was necessary to center the pre- and intraoperative image series about the same point and correct for scaling (based on supplied voxel dimensions). The automated system first resampled both datasets to have isotropic voxels matching the in-plane voxel dimension of the preoperative datasets (usually $\sim$0.39 mm). The system then computed the center of mass of the 1.5 and 0.5 T segmented datasets using the total gland (TG) voxels and translated (without rotation) the datasets in order to center them about the same voxel.

The three-dimensional image matching system described in Refs. 10, 13 was then used to perform deformable registration on the datasets. In summary, the method involves the following steps: (1) a finite element model with tetrahedral elements is created from the segmented images derived from the initial preoperative 1.5 T scans; (2) the central gland and peripheral zone are labeled separately within the mesh, allowing different material properties to be assigned to each

region (Fig. 2); (3) the boundary surface is extracted from this mesh and is treated as an elastic membrane that is deformed iteratively in three dimensions so as to match the corresponding boundary of the segmented (TG) datasets derived from the 0.5 T intraoperative scans, using an active surface algorithm described in Ref. 14; (4) the surface deformations from step (3) are used as inputs in the finite element model so as to infer a volumetric deformation field; and (5) the volumetric deformation field from the previous step is interpolated onto the original image grid (either the segmented or original gray scale image dataset).

Thus, the modeling system accepts as input segmentations of the CG and PZ from the preoperative (1.5 T) dataset as well as segmentations of *only* the TG at 0.5 T. A three-dimensional mesh model (containing representations of the CG and PZ) derived from the 1.5 T label dataset is deformably registered with the surface of the 0.5 T dataset. The resultant deformation field is applied to the original 1.5 T label dataset, thus producing deformed preoperative label images whose contours are now registered with the intraoperative images, and in which the inferred relative position of internal features (i.e., CG/PZ interface) are displayed (see later). Applying the same deformation field to the original 1.5 T gray scale images produces deformed MR images in which corresponding internal anatomic positions are registered between pre- and intraoperative datasets.

The finite element modeling system described above is based upon an isotropic, linearly elastic material framework (discussed below, and see Ref. 10). Such materials are characterized by two parameters: Young's elastic modulus E and Poisson's ratio ν. Young's modulus is the elastic modulus for tensile stress, and represents the ratio of stress (force per area) to strain (fractional increase in length) in the direction of the load for a given material. Poisson's ratio is the ratio of the strain perpendicular to the applied load (lateral strain) to the strain in the direction of the applied load (axial strain). Together, these parameters determine the elastic properties of the material being modeled. In our model, the CG and PZ are segmented as separate structures, and a tetrahedral mesh is generated for each, sharing common mesh nodes at the common boundary. An inhomogeneous linearly elastic model of behavior under deformation is obtained by selecting different values of Young's modulus and Poisson's ratio for the mesh elements of the CG and the mesh elements of the PZ. Although the choice of these parameters is critical to the reliability of a physics-based biomechanical model, they have not, to our knowledge, been determined experimentally or numerically for prostate tissues.

Consequently, the values of E and ν used in the biomechanical deformation model were chosen based upon our prior experience with brain modeling. Using a starting value of $E = 3$ kPa and $\nu = 0.4$ (appropriate for brain parenchyma[10]), trial registrations were made iteratively on a single case and the results inspected at different values of E and ν. It became apparent from initial runs that the observable deformation of the CG and PZ varied considerably, with the PZ experiencing greater deformation. By separately varying the values of the parameters for the CG and PZ, a set of
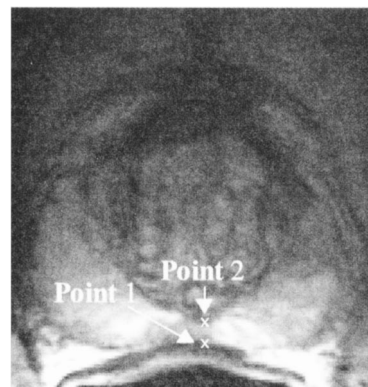

FIG. 3. An illustration depicting the manually selected points in the point-based validation experiment (a zoomed 1.5 T image is shown). As described in the text, points 1 and 2 were selected in the posterior aspect of the PZ and CG, respectively, near the midline. Midline structures and local image characteristics (e.g., a nodule of benign prostatic hyperplasia) were used for reference in selecting the points in corresponding images.

values was obtained [CG: $E = 30$ kPa and $\nu = 0.2$; PZ: $E = 3$ kPa and $\nu = 0.4$], which produced the most anatomically consistent results, and was held fixed for all trials. A more rigorous choice of parameters would require *in vivo* experimental studies (ideally) or numerical studies to determine these values for prostate tissues (see the Discussion).

Experiment protocol

It is first necessary to validate the dataset of multiply (manually) segmented prostate glands (TG and CG/PZ) from the pre- and intraoperative imaging sessions to establish that this can be done reliably in both image datasets. In order to evaluate the agreement in any pair of repeated measures using two independent two-dimensional segmentation occasions, a measure of similarity between two segmentations was adopted. For voxel-by-voxel classification agreement, as is necessary for a comparison of MRI segmentation datasets, the Dice similarity coefficient (DSC) has been employed.[15,16] The DSC is given by

$$\text{DSC} = \frac{2a}{2a+b+c} = \frac{2n\{A_1 \cap A_2\}}{n\{A_1\} + n\{A_2\}}, \qquad (1)$$

where a is the number of voxels common to (shared by) both datasets; b is the number of voxels unique to the first dataset; c is the number of voxels unique to the second dataset; A_1 and A_2 are the set of voxels identified as signal in the first and second dataset, respectively, and; $n\{A\}$ is the number of elements in set A. It has been shown that the DSC may be interpreted as a special case of the widely used Kappa coefficient (see Refs. 15, 17, and 18). The DSC is appropriate in comparison-of-agreement studies, and has been employed in previous studies of this nature,[17] including, specifically, segmentation agreement.[15] It is generally accepted that a value of DSC > 0.7 represents excellent agreement.[15]

Next, the difference in quality of the match between pre- and intraoperative datasets as a result of the deformable registration system was assessed. The DSC for the 0.5 T "stan-

dard'' and the undeformed and deformed 1.5 T segmentations was computed, separately for TG, CG, and PZ before and after deformable registration. Similar analyses comparing the volume of TG, CG, and PZ were carried out.

As an additional measure of deformable registration accuracy, two sets of points were manually selected in corresponding midaxial slices of the rigidly registered pre- and intraoperative scans in each of the ten cases. These points were selected in consultation with an expert in pelvic imaging, using the image display and navigation software described in Ref. 12. In the 1.5 T dataset, the first point (Point 1) was selected at the posterior border of the PZ near the midline and the second point (Point 2) was selected at the posterior border of the CG near the midline (Fig. 3). The corresponding points in the 0.5 T images were selected using standard midline structures (such as the pubic symphysis) as well as patient-specific local image intensity characteristics (e.g., such as a local nodule of benign prostatic hyperplasia, etc.) for reference. The movement of the manually placed landmarks in the deformed (by our algorithm) preoperative data was tracked. The distance between the corresponding identified points in the 0.5 T dataset and the undeformed and deformed preoperative 1.5 T images was measured and compared. As a measure of within-case variability, one case was selected at random and the measurements were repeated on the five separate runs of the modeling system (based on the five separate segmentations).

Statistical methods

Assessment of segmentation agreement

In order to validate our multiply segmented 1.5 T (''MRI'') and 0.5 T (''MRT'') datasets, we conducted an agreement-of-repeated-segmentations study. We labeled 10 segmentation pairs from the 5 segmentation occasions as 1–2, 1–3, 1–4, 1–5, 2–3, 2–4, 2–5, 3–4, 3–5, 4–5 (indicating every possible combination of segmentations). For each of the 12 combinations of operators (1 and 2), imaging (MRI and MRT), and segmentation of the gland (CG, PZ, and TG), summary statistics such as the mean and standard deviation of DSC values over the cases were calculated. Based on these statistics, a 95% confidence interval was constructed separately for each of the segmentation pairs and for each case. Because any DSC value was restricted between 0 and 1, but tended to vary close to 1, a log transformation of the DSC value was used and the confidence interval was first constructed in the log space and then transformed to the restricted DSC space. Here we did not pool the cases of the two operators, with the consideration that these operators might have different underlying reliability results. The intraclass correlation coefficient[19] for measuring agreement within any segmentation pair was computed. Additionally, a two-way analysis of variance (ANOVA) F test was conducted to assess the statistical significance of the effects of case or segmentation occasion on the disagreement in any segmentation pair.

TABLE I. Interoperator agreement study, summarizing the correspondence (DSC) after repeat segmentation of the prostate and its substructures. *Note:* p values <0.005 in all hypothesis tests for mean DSC>0.70 in each segmentation pair. DSC—dice similarity coefficient; CG—central gland; PZ—peripheral zone; TG—total gland.

Operator	Method	Region	Mean (95% CI) DSC	p Segmentation	p Case
1	1.5T MRI	TG	0.95 (0.92, 0.97)	0.15	<0.005
		CG	0.93 (0.89, 0.96)	0.30	<0.005
		PZ	0.86 (0.80, 0.92)	0.16	<0.005
	0.5T MRI	TG	0.94 (0.91, 0.95)	0.64	<0.005
		CG	0.91 (0.85, 0.94)	0.72	<0.005
		PZ	0.82 (0.77, 0.87)	0.31	<0.005
2	1.5T MRI	TG	0.96 (0.95, 0.97)	<0.005	<0.005
		CG	0.94 (0.92, 0.96)	0.18	<0.005
		PZ	0.90 (0.86, 0.94)	0.09	<0.005
	0.5T MRI	TG	0.94 (0.89, 0.97)	0.58	<0.005
		CG	0.91 (0.82, 0.97)	0.49	<0.005
		PZ	0.85 (0.78, 0.91)	0.04	<0.005

Assessment of registration agreement

Because the above validation study did not indicate a significant difference in segmentation occasions by the two operators, all ten cases were pooled in the subsequent analysis and comparison of pre- and intraoperative results. For each of the six combinations of methods (MRI and MRT) and segmentation of the gland (CG, PZ, and TG), summary statistics of the DSC measures, as well as a 95% confidence interval were reported separately for the shapes with and without (finite element-based) deformation. The statistical hypothesis that the mean DSC was improved after finite element-based deformation of the gland was tested using a one-sided paired t test. The case effects were also evaluated using a stratified analysis by case. Finally, a two-way ANOVA with case replicates was used to assess the statistical significance of the effect of shape (with and without deformation) and the effect of case on the DSC values.

In the analysis of volume for CG and PZ pooled over all ten cases, a log transformation was first applied to symmetrize the data and for variance stabilization. Summary measures and a two-way ANOVA were calculated to assess and compare the volume due to either the shape effect with and without deformation or to the case effect.

In the point-tracking experiment, summary statistics (mean, standard deviation, and range) of the displacements (mm) of points 1 and 2 in the undeformed and deformed preoperative images as compared to the corresponding points in the target (intraoperative) images have been computed. In addition, paired t tests were performed to assess whether the distance between the corresponding points was reduced after deformable registration. In the repeated-measurement experiment, the reproducibility of the measurements was assessed by computing the coefficient of variation (the ratio of the standard deviation to the mean).

RESULTS

Assessment of segmentation agreement

The mean DSC values over ten segmentation occasions and five cases for each operator are presented in Table I. All

TABLE II. Mean Dice similarity coefficient of undeformed 1.5 T MRI and deformed 1.5 T MRI using 0.5 T intraoperative MRI as standard. *Note:* p values <0.005 for all hypothesis tests evaluating whether the mean DSC of the undeformed group is less than the mean DSC of the deformed group. CG—central gland; PZ—peripheral zone; TG—total gland.

Region	Mean (95% CI) DSC of undeformed data using 0.5 T MRI as standard	Mean (95% CI) DSC of deformed data using 0.5 T MRI as standard
TG	0.81 (0.68, 0.94)	0.94 (0.89, 0.99)
CG	0.78 (0.63, 0.93)	0.86 (0.77, 0.95)
PZ	0.59 (0.40, 0.79)	0.76 (0.62, 0.91)

95% confidence intervals had lower bounds above 0.70, with the latter DSC value used as the benchmark value for excellent agreement.[15,20] As expected, all underlying mean DSC values were statistically significantly greater than 0.70, based on one-sided paired t tests ($p<0.005$). Segmentation agreement results for TG (mean DSC ranged 0.94–0.96) were slightly greater than those for CG (mean DSC ranged 0.91–0.94), which, in turn, were greater than those for PZ (mean DSC ranged 0.82–0.90). We also obtained fair to good estimated intraclass correlation coefficients, ranging from 0.46–0.77 for the first operator and 0.34–0.85 for the second operator, as measures of intersegmentation agreement.

The ANOVA F tests suggested that the effect due to repeated segmentation occasions was not statistically significant for most cases, except for 1.5 T MRI+TG ($p<0.005$) and for 0.5 T MRI+PZ ($p=0.04$) by the second operator. This suggested that there was slight operator variability in the segmentation performances. In addition, the effect due to case was statistically significant ($p<0.005$) for all combinations. This may explain some of the operator variability.

Assessment of registration system

The registration strategy described above was run on each of the five (repeat) segmented datasets derived from each of the ten cases. In each case, the TG contour of the pre and intraoperative datasets was used for the initial rigid registration. Following this, tetrahedral meshes of the CG and PZ based on the preoperative segmentations were created. The mean edge length, corresponding to the discretization step, was approximately 2.0 mm (in our method, the number of elements is higher at the boundary, so the edge length varied between approximately 0.1 and 3.9 mm). Surface matching between the preoperative surface and the intraoperative TG boundary was performed, and the result of this served as a boundary condition for the calculation of the volumetric deformation field. The volumetric deformation field calculated from the modeling system was then applied to the preoperative gray scale and segmented (CG/PZ) datasets, producing deformed (matched) gray scale and segmentation data. Using current versions of our software, the entire program runs in approximately 6 mins, with approximately 2 mins necessary for the rigid registration and resampling steps; 2 min for the active surface matching; and under 2 min to calculate and apply the volumetric deformation field (Ultra 80, 450 MHz Ultra SPARC-II; Sun Microsystems; Mountainview, CA.)

The similarity results over all ten cases are shown in Table II. Without finite element-based deformable registration (but following a center-of-mass-based rigid registration), the mean DSC values were 0.81, 0.78, and 0.59 for TG, CG, and PZ, respectively. By comparison, after deformable registration, higher mean DSC values were observed: 0.94, 0.86, and 0.76, respectively. When comparing the underlying mean DSC values with and without deformation for all areas of the prostate, one-sided t tests showed that the DSC values were statistically significantly improved when deformable registration was applied ($p<0.005$). These improvements occurred in all tested cases and repetitions. The ANOVA F tests confirmed that shape had a statistically significant effect on
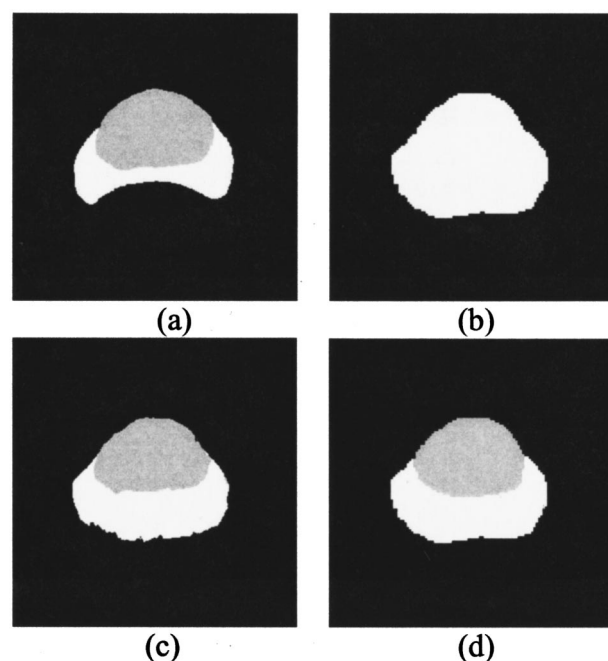

FIG. 4. A typical axial slice demonstrating the deformable registration system. Initial rigid alignment is provided by a center-of-mass-dependent process described in the text. (a) is the segmented 1.5 T image, showing the CG (gray) and PZ (white). (b) is the segmented 0.5 T intraoperative image in the corresponding slice plane. Note that the modeling system receives as input segmentations from 1.5 T with the CG/PZ boundary, but only the TG contour of the 0.5 T series. (c) shows the deformed 1.5 T image with the segmentation (i.e., CG/PZ boundary) inferred via application of the computed deformation map. For comparison, (d) is the same image as (b), with the CG/PZ interface segmented by a human observer (the standard in statistical tests). Note the agreement between (c) and (d).
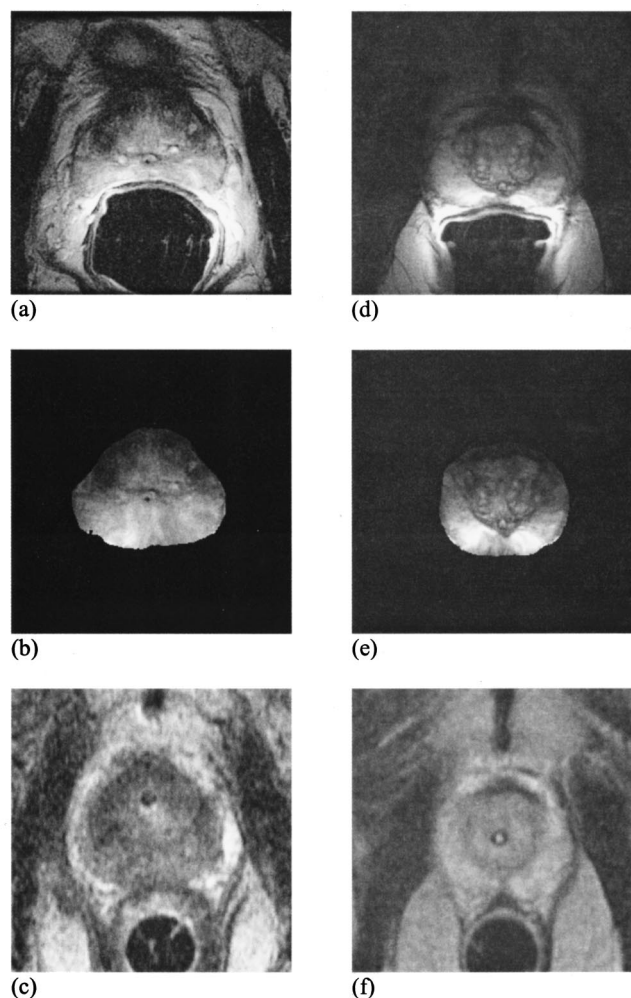
FIG. 5. (a)–(c) depict the application of the calculated volumetric deformation field from the case presented in Fig. 4 to the original 1.5 T gray scale image. (a) is the original 1.5 T image [from which (a) in Fig. 4 was derived]. (b) is the deformed gray scale image [corresponding to (c) in Fig. 4]. (c) is the 0.5 T slice [corresponding to (b) and (d) in Fig. 4]. (d)–(f) are a similar series of (d) preoperative, (e) deformed preoperative, and (f) intraoperative images from another case. Note the match between (b) and (c); and (e) and (f). Note also the poorer resolution and more difficult delineation of the CG and PZ boundaries in the intraoperative 0.5 T image. Reasons for the variability in the intraoperative appearance of the PZ are discussed in the text.

the DSC values ($p < 0.005$). As before, the case effect was also significant ($p < 0.005$).

Figures 4 and 5 highlight typical results from the experiment, demonstrating the output of the deformable registration method. Figure 4 shows the inferred CG and PZ bound-

aries and Fig. 5 illustrates the deformed preoperative gray scale image registered so as to match the three-dimensional surface contour of the intraoperative image series.

The volume results over all ten cases are summarized in Table III. For the CG, the means of volume were (preoperatively) 28.36 cm^3 without deformation, 28.49 cm^3 with deformation, and 27.68 cm^3 under 0.5 T MRI (intraoperatively), respectively. For PZ, the means of volume were (preoperatively) 16.85 cm^3 without deformation, 17.26 cm^3 with deformation, and 19.58 cm^3 under 0.5 T MRI (intraoperatively), respectively. Paired t tests suggested that the deformable registration system did not statistically significantly change the mean volume results. However, the effect of case was statistically significant ($p < 0.005$) in each structure.

Summary results of the manually identified point tracking experiment are given in Table IV. As shown, the mean distance between point 1 (the point at the PZ border) identified in the rigidly registered 1.5 and 0.5 T images was 4.20 mm. This mean distance was reduced to 1.01 mm after deformable registration. For point 2 (an internal point on the posterior border of the CG), the mean distance changed from a prematched value of 1.76 to 0.73 mm after deformable matching. Also of interest, the maximum displacements of points 1 and 2 changed from 5.97 and 3.50 mm to 2.30 and 1.56 mm, respectively, following deformable registration. The repeated-measurement experiment conducted on a single case gave consistent results, yielding coefficients of variation of less than 0.20 for all measurements, indicating satisfactory reproducibility.

DISCUSSION

We have created and validated a retrospective dataset of segmented prostate glands from pre- and intraoperative studies of patients who previously underwent MR-guided prostate brachytherapy. Using an automated system, these data series were registered by translating them to align corresponding centers of mass, and deformed using a 3-D finite element-based biomechanical modeling system. The model was successfully applied to two different sets of five cases, each set segmented by an independent operator five times. This approach simulates multiple repetitions of five different brachytherapy cases for two independent operators, allowing effective preliminary testing of the model.

So far, very little work has been done to develop registration systems for prostate images obtained in US, CT, x-ray, or MR. Manual matching with visible landmarks (i.e., anatomical or treatment seeds), has been used to match US to

TABLE III. A comparison of preoperative undeformed, deformably registered, and intraoperative CG and PZ volumes. *Note:* CG—central gland; PZ—peripheral zone; TG—total gland.

Region	Mean volume (95% CI) (cm^3) Undeformed 1.5 T MRI	Mean volume (95% CI) (cm^3) Deformed 1.5 T MRI	Mean volume (95% CI) (cm^3) 0.5T MRI	p^a
CG	28.36 (23.53, 33.19)	28.49 (23.62, 33.35)	27.68 (22.79, 32.57)	0.68
PZ	16.85 (15.90, 17.79)	17.26 (15.92, 18.60)	19.58 (18.02, 21.14)	0.23

[a]Hypothesis testing for equivalence between undeformed and deformed volumes did not yield a statistically significant volume change.

TABLE IV. The distance between manually placed and deformed landmarks in preoperative images compared to corresponding points in intraoperative images.

Point	Mean distance in mm between the point in undeformed preoperative and intraoperative images (SD) (range)	Mean distance in mm between the point in deformed preoperative and intraoperative images (SD) (range)	p^a
1	4.20 (1.26) (1.95, 5.97)	1.01 (0.56) (0.47, 2.30)	<0.005
2	1.76 (0.73) (0.78, 3.50)	0.73 (0.40) (0, 1.56)	<0.005

[a]Paired *t* tests showed that the linear distance in mm between the landmarks and the target position in the intraoperative image was lower in the deformed as compared to the undeformed dataset for both sets of points.

CT[6] and radiographs to MR[21] to assess post-implant dosimetry, as well as to match CT to MR for the assessment of conformal radiation therapy.[7] However, these were inherently manual approaches, and required visible landmarks. In the analysis by van Herk,[8] rigid registration (translation and rotation) of the prostate in MR and CT studies was achieved using a chamfer matching technique. In this study, the poorer quality of prostate matching as compared to bone was attributed to shape differences of the gland, or segmentation error. However, the observed shape changes were sufficiently small that consistent results were obtained using a rigid registration system. It must be noted that in van Herk's study, the patient position was fixed (supine) and the endorectal coil and rectal obturator were not employed. These factors apparently contribute to the large shape changes that we have observed between pre- and intraoperative prostate imaging.[9]

Our rigid registration strategy consisted of translation without rotation because in our datasets, rotations about the base–apex and anterior–posterior axes were not observed. However, it is possible that some degree of rotation occurred about the left-right axis (i.e., a forward roll), or that a combination of rotation and deformation occurred. Unfortunately, using current imaging systems, it is not possible to distinguish these components with certainty. Although a visual inspection of the rigidly registered datasets suggested that our approach was satisfactory, it is nevertheless important to note that our modeling system will explain changes in shape as a deformation. Other systems that compute rigid registrations with only free rotation may equally explain deformation changes as rotation. Future advances in high resolution pelvic imaging may clarify this.

To our knowledge, our study represents the first time that a biomechanical finite element-based deformable registration system has been applied to prostate image data. Since the modeling system is able to infer volumetric deformation based upon surface displacements, it is not necessary to quantify the potentially numerous surface-acting forces that may be responsible for the gland's deformation. Another advantage of the method is that surface correspondences are determined automatically during the active surface matching (based on TG contours); consequently, the manual selection of individual correspondences (which is subject to human error) is not required.

A limitation of the current registration method is that it uses a linearly elastic and isotropic framework. The assumption of tissue isotropy has never been tested for the prostate. In addition, the choice of a linear elasticity framework may

not be ideal due to the large deformations encountered (notwithstanding the matching results noted above).

Although the model permits tissue inhomogeneity (the separate selection of Young's modulus and Poisson's ratio) for the CG and PZ, the choice of parameters was restricted by the paucity of literature dealing with the *in vivo* assessment of prostate biomechanical tissue properties (as mentioned earlier). While experimental and numerical work has been done to estimate E and ν for the brain[22] and some other tissues, to our knowledge these parameters are not known for prostate tissues. As discussed, the choice of parameters was determined by varying the values of E and ν on a single case, and identifying the parameters that gave the most anatomically accurate matching results (held fixed for subsequent trials).

The parameters used for the PZ are similar to those selected by others for brain parenchyma.[23] The values selected for the CG reflect a higher E (consistent with a stiffer tissue[23]) and a smaller ν (possibly a result of fluid movement or tissue changes). However, it is extremely important to note that in this study, the selected values for E and ν represent the macroscopic behavior of the entire tissue in our modeling system, but may not be representative of the microscopic properties of the tissue itself. These parameters are better regarded as "apparent" values that were selected on the basis of image match quality (see Ref. 24, where apparent ν values were selected based on anatomical variability). Although the selected parameters gave coherent results in our experiments, further validation with higher resolution imaging or experimentation is required.

Significant volume changes did not occur, despite the fact that the ν values are not 0.5. This result is related to the fact that the preoperative TG surface is matched to the intraoperative TG boundary (active surface match). This constrained the volume change of the deformed preoperative TG, allowing the algorithm to correctly represent the biomechanical topology of the gland. Thus, the choice of tissue parameters had a greater effect on final node position than cell size. However, current limitations in image contrast and resolution will influence the accuracy of volume measurements in this study.

Area-based and point-based measures were used to assess the accuracy of the deformable registration system. One difficulty in assessing registration is that the highest resolution imaging occurs in the preoperative setting. However, it is the conformation of the gland in the intraoperative setting that is most important for procedure planning. Thus, the intraopera-

tive appearance of the gland must serve as the standard to which matching results are compared. Using preoperative T2-weighted MR imaging with an endorectal coil, the TG contour, as well as that of the CG, PZ, and in many cases, tumor foci can be identified. In the intraoperative imaging, the TG is still relatively easy to identify. The CG and PZ also *can* be identified, however, the segmentation is more difficult because of the relatively poorer soft tissue contrast and resolution (related to the lower field strength; see Fig. 5). Substructure delineation at low-field (0.5 T) strength is particularly difficult if there is diffuse T2 hypointensity of the PZ, due to tumor, prior external beam or interstitial radiation therapy, hormonal therapy, or prostatitis (the latter three factors were excluded in our study). This variability can be seen by comparing Figs. 5(c) and 5(f) (from different patients).

This motivates our desire to predict internal anatomy and deformation based on changes in the TG contour. To assess this, segmentation agreement was measured before and after deformable registration (Table II) using a previously described similarity measure (Refs. 15 and 25). Although the "ground truth" in this experiment was the manual segmentation of the CG and PZ from 0.5 T imaging (where a substructure can be difficult to identify), this was necessary in order to verify the accuracy of the output. This approach also has the advantage of comparing registration accuracy over the entire gland. Further validation was conducted by tracking the displacement between manually identified corresponding points before and after deformable registration (Table IV).

These experiments showed that by applying a deformable registration system, it is possible to significantly improve the correspondence between MR images obtained pre- and intraoperatively, when compared to rigid registration alone. Essentially, this can result in higher "information-content" 0.5 T images, which combine the additional detail seen at 1.5 T with the convenience of intraoperative imaging. In addition, the CTV (the PZ) can be predicted in every slice based upon surface contour displacements using this approach. Consequently, a segmentation of the PZ made on the high-resolution preoperative data series can be mapped onto the intraoperative dataset, potentially improving the accuracy and speed of delineating the CTV intraoperatively. The total time consumption of the process (approximately 6 min) should be satisfactory for intraprocedure use; however, further speed improvements are expected based on hardware improvements and optimization of the software (particularly its parallel implementation).

It must be noted that the region of the gland with poorest agreement prior to deformable registration was the PZ. In our experiments, this region had a mean DSC value of 0.59 (following rigid registration using the center-of-mass), which is lower than the (DSC>0.7) criteria set out for excellent agreement in Refs. 15 and 20. As this region is the CTV for MR-guided brachytherapy, this is the region of the gland that must be accurately delineated. Following deformable registration, the mean DSC value for the PZ rises to 0.76, representing a statistically significant increase ($p < 0.005$). Thus,

it appears that the method is able to significantly improve the quality of the match for the CTV.

Although in this study we demonstrate the application of this modeling approach for 1.5 on to 0.5 T MR deformable registration, the approach clearly has implications for multi-modality (i.e., MR, MR-spectroscopy, etc.) image registration and fusion. In particular, preoperative MR to intraoperative ultrasound image fusion could substantially improve the information content of intratreatment imaging. Finally, since this approach allows us to infer the location of internal anatomical features, it has a potential application in delineating the location of tumor foci for highly targeted image-guided therapy in which intraoperative imaging may not be able to adequately resolve the region of interest.

CONCLUSIONS

To increase the accuracy of intraprocedure navigation, one of our objectives has been to increase the information content of images obtained under real-time guidance. We have retrospectively demonstrated a method that increases the information content of intraoperative prostate imaging using high resolution preoperative data. The method matches preoperative high-resolution images to intraoperative images, using an initial rigid and then a nonrigid, finite element-based registration strategy. Applying the matching system prospectively can next test the utility of this method to facilitate accurate identification of the CTV during brachytherapy sessions. The ultimate goal of such methodologies is to be able to identify the target in a highly accurate fashion using matched preoperative imaging, and then to deliver highly localized therapy under real-time guidance.

ACKNOWLEDGMENTS

a)Correspondence: Clare M.C. Tempany, M.D., MRI Division, Department of Radiology, Brigham and Women's Hospital, L1-050, 75 Francis St., Boston, Masachusetts 02115. Telephone (617) 732-7858; fax: (617) 582-6033; electronic mail: ctempany@bwh.harvard.edu
[1] "Cancer facts and figures," American Cancer Society, Atlanta, Georgia 1997.
[2] J. A. Talcott, P. Rieker, J. A. Clark, K. J. Propert, J. C. Weeks, C. J. Beard, K. I. Wishnow, I. Kaplan, K. R. Loughlin, J. P. Richie, and P. W. Kantoff,

"Patient-reported symptoms after primary therapy for early prostate cancer: results of a prospective cohort study," J. Clin. Oncol. **16**, 275–1283 (1998).

[3] A. V. D'Amico, R. Cormack, C. M. Tempany, S. Kumar, G. Topulos, H. M. Kooy, and C. N. Coleman, "Real-time magnetic resonance image-guided interstitial brachytherapy in the treatment of select patients with clinically localized prostate cancer," Int. J. Radiat. Oncol., Biol., Phys. **42**, 507–515 (1998).

[4] D. Cheng and C. Tempany, "MR imaging of the prostate and bladder," Semin Ultrasound CT MR **19**, 67–89 (1998).

[5] M. L. Schiebler, M. D. Schnall, H. M. Pollack, R. E. Lenkinski, J. E. Tomaszewski, A. J. Wein, R. Whittington, W. Rauschning, and H. Y. Kressel, "Current role of MR imaging in the staging of adenocarcinoma of the prostate," Radiology **189**, 339–352 (1993).

[6] V. Narayana, P. L. Roberson, R. J. Winfield, and P. W. McLaughlin, "Impact of ultrasound and computed tomography prostate volume registration on evaluation of permanent prostate implants," Int. J. Radiat. Oncol., Biol., Phys. **39**, 341–364 (1997).

[7] K. Kagawa, W. R. Lee, T. E. Schultheiss, M. A. Hunt, A. H. Shaer, and G. E. Hanks, "Initial clinical assessment of CT–MRI image fusion software in localization of the prostate for 3D conformal radiation therapy," Int. J. Radiat. Oncol., Biol., Phys. **38**, 319–325 (1997).

[8] M. van Herk, A. Bruce, A. P. Kroes, T. Shouman, A. Touw, and J. V. Lebesque, "Quantification of organ motion during conformal radiotherapy of the prostate by three dimensional image registration," Int. J. Radiat. Oncol., Biol., Phys. **33**, 1311–1320 (1995).

[9] M. Hirose, A. Bharatha, N. Hata, S. K. Warfield, and K. H. Zou, "Quantitative MRI assessment of prostate gland deformation before and during MRI-guided brachytherapy," Radiological Society of North America (RSNA) Annual Meeting, 25–30 November, 2001.

[10] M. Ferrant, S. Warfield, A. Nabavi, B. Macq, and R. Kikinis, *Registration of 3D Intraoperative MR Images of the Brain Using a Finite Element Biomechanical Model*, edited by A. M. DiGioia and S. Delp, presented at the 3rd International Conference on Medical Image Computing and Computer-assisted Intervention (MICCAI), Pittsburgh, PA, 2000 (Heidelberg, Springer-Verlag, 1999), pp. 19–28.

[11] J. F. Schenck *et al.*, "Superconducting open-configuration MR imaging system for image-guided therapy," Radiology **195**, 805–814 (1995).

[12] D. Gering, A. Nabavi, R. Kikinis, W. E. L. Grimson, N. Hata, P. Everett, F. Jolesz, and W. Wells III, *An Integrated Visualization System for Surgical Planning and Guidance Using Image Fusion and Interventional Imaging*, edited by C. Taylor and A. Colchester, presented at the 2nd International Conference on Medical Image Computing and Computer-Assisted Intervention (MICCAI), Cambridge, England, 1999 (Heidelberg, Springer-Verlag, 1999), pp. 809–819.

[13] S. Warfield, M. Ferrant, X. Galle, A. Nabavi, F. A. Jolesz, and R. Kikinis, *Real-time Biomechanical Simulation of Volumetric Brain Deformation for Image Guided Neurosurgery*, presented at the High Performance Networking and Computing Conference, Dallas, 2000.

[14] M. Ferrant, B. Macq, A. Nabavi, and S. K. Warfield, *Deformable Modeling for Characterizing Biomedical Shape Changes*, edited by G. Borgefors, I. Nystrom, and G. Sanniti di Baja, DGCI2000: Discrete Geometry for Computer Imagery, Uppsala, Sweden, 2000 (Heidelberg, Springer, 2000), pp. 235–248.

[15] A. P. Zijdenbos, B. M. Dawant, R. A. Margolin, and A. C. Palmer, "Morphometric analysis of white matter lesions in MR images: Method and validation," IEEE Trans. Med. Imaging **13**, 716–724 (1994).

[16] L. R. Dice, "Measures of the amount of ecologic association between species," Ecology **26**, 297–302 (1945).

[17] J. L. Fleiss, "Measuring agreement between two judges on the presence or absence of a trait," Biometrics **31**, 651–659 (1975).

[18] L. Hubert, "Kappa revisited," Psychol. Bull. **84**, 289–297 (1977).

[19] K. H. Zou and M. P. McDermott, "Higher-moment approaches to approximate interval estimation for a certain intraclass correlation coefficient," Stat. Med. **18**, 2051–2061 (1999).

[20] J. J. Bartko, "Measurement and reliability: statistical thinking considerations," Schizophr Bull. **17**, 483–489 (1991).

[21] M. A. Moerland, H. K. Wijrdeman, R. Beersma, C. J. Bakker, and J. J. Battermann, "Evaluation of permanent I-125 prostate implants using radiography and magnetic resonance imaging," Int. J. Radiat. Oncol., Biol., Phys. **37**, 927–933 (1997).

[22] A. Hagemann, K. Rohr, H. S. Stiehl, U. Spetzger, and J. M. Gilsbach, "Biomechanical modeling of the human head for physically based, non-rigid image registration," IEEE Trans. Med. Imaging **18**, 875–884 (1999).

[23] M. I. Miga, D. W. Roberts, F. E. Kennedy, L. A. Platenik, A. Hartov, K. E. Lunn, and K. D. Paulsen, "Modeling of retraction and resection for intraoperative updating of images," Neurosurgery **49**, 75–84 (2001).

[24] J. Rexilius, S. K. Warfield, C. R. G. Guttmann, X. Wei, R. Benson, L. Wolfson, M. Shenton, H. Handels, and R. Kikinis, *A Novel Nonrigid Registration Algorithm and Applications*, edited by W. J. Niessen and M. A. Viergever, presented at the 4th International Conference on Medical Image Computing and Computer-Assisted Intervention (MICCAI), Utrecht, The Netherlands, 2001 (Heidelberg, Springer-Verlag, 2001), pp. 923–931.

[25] K. Van Leemput, F. Maes, D. Vandermeulen, and P. Suetens, "Automated model-based tissue classification of MR images of the brain," IEEE Trans. Med. Imaging **18**, 897–908 (1999).